Physical and Electrochemical Characterization of Aluminium Electrodes During Electrocoagulation

Chia Miang Khor[1], Michael Evan Liao[2], Arpita Iddya[1], Shengcun Ma[1], Fan Yang[1], Yu-Hsuan Liu[3], Yousuf Z. Bootwala[4], Gyoung Gug Jang[5], Fan Yang[1], Mark S Goorsky[2], Eric M. V. Hoek[6,7], Costas Tsouris[4], Jim Mothersbaugh[8], Marta C. Hatzell[4] and David Jassby[6]

1 Department of Civil and Environmental Engineering, University of California, Los Angeles, CA 90095, USA.

2 Department of Material Science and Engineering, University of California, Los Angeles, CA 90095, USA.

3 School of Civil and Environmental Engineering, Georgia Institute of Technology, Atlanta, GA, 30332 USA

5 Manufacturing Science Division, Oak Ridge National Laboratory, Oak Ridge, TN, 37830 USA

6 Department of Civil & Environmental Engineering, Institute of the Environmental & Sustainability and California NanoSystems Institute, University of California, Los Angeles, CA, 90095 USA

7 Lawrence Berkeley National Labarotory, Berkley, CA, 94709 USA

8 Water Tectonics, Everett, WA 98203

4 George W. Woodruff School of Mechanical Engineering, Georgia Institute of Technology, Atlanta, GA, 30332 USA

Abstract

Electrocoagulation (EC) of synthetic groundwater was conducted using an aluminium electrode in a flow-by reactor under varying hydrodynamic and electrochemical conditions. Treated water achieved silicate removal of up to 50 ± 4%, and hardness removal of 11 ± 1 %. Physical, chemical, and electrochemical characterization was performed to explore changes in electrode surface morphology/composition. Electrochemical impedance spectroscopy (EIS) showed that reactions at the electrode/water interface are sensitive to changes in the immediate environment. We demonstrate that the most energy intensive step in EC is aluminium dissolution at the anode, which remained fairly constant due to the continuous renewal of the surface, a result of aluminum dissolution. At the cathode, a structural change in the oxide layer, from γ-Al_2O_3 to Gibbsite, was detected by grazing-incidence X-ray diffraction, which decreased the resistance to charge transfer at the cathode, resulting in decreased electrode resistance. Higher shear rates in the system minimize the accumulation of aluminium hydroxide solids and aluminium ions at the electrode/water interface, minimizing the formation of thick scalants and amorphous $Al(OH)_3$ on the cathode and anode, respectively. It was further demonstrated by EIS that under these conditions the resistance to charge transfer was constant throughout the duration of the experiment.

Keywords: Electrocoagulation, hardness and silicate removal, electrochemical characterization, aluminium oxide speciation

Synopsis: Dynamic electrochemical conditions along the cathode during electrocoagulation impact the resistance to charge transfer and increase the performance of the process.

Introduction

Groundwater accounts for 29% of the freshwater supply in the USA [1], with 41% of the USA population regularly depending on groundwater for their drinking needs. A multitude of water purification methods exist for the treatment of groundwater for potable applications. While membrane separation techniques such as reverse osmosis and nanofiltration are effective for the removal of salinity and ppm levels of unwanted substances [2-4], they are susceptible to fouling, and in particular to mineral scaling while treating groundwater with high mineral content [5-8]. Traditionally, a pre-treatment step that involves coagulation/flocculation is often necessary to remove contaminants such as suspended solids and dissolved organic carbon [9-12].

Coagulation can be achieved through either chemical addition or electrocoagulation (EC). In chemical coagulation, metal salts (e.g., $Al_2(SO_4)_3$, $FeCl_3$) are added to the groundwater where they rapidly form metal hydroxide species that neutralize charges, form flocs, and promote the removal of contaminants [13-15]. Often, it is difficult to estimate a suitable dosage of chemicals to effectively treat the water, resulting in extensive trial-and-error testing to find an appropriate dosage [16, 17]. In addition, due to metal-induced water hydrolysis, the pH of the water can rapidly become acidic, which requires adjustment and/or limits the amount of coagulants that can be used. [17, 18]. Furthermore, the addition of coagulant salts and alkalizing agents (e.g., NaOH) to the water can lead to a significant increase in the salinity of the water, although this is only an issue when large quantities of coagulants are used [19, 20].

EC is an alternative process to chemical coagulation where instead of dosing chemical coagulants, sacrificial metal anodes (often aluminium or iron) are intentionally dissolved/corroded into the water through electrochemical oxidation to produce the coagulating species. At the cathode, water electrolysis generates hydroxide ions and H_2 gas, with the generated hydroxide ions compensating for any hydroxide consumption by the dissolved metal ions (e.g., Al^{+3}) to form insoluble metal hydroxide solids. As a result, the pH of the water remains stable, regardless of the coagulant loading [21-23]. Because of its pH stability, EC allows for far higher coagulant dosing compared to chemical coagulation, as comparable loading using chemical coagulation would dramatically reduce the pH of the stream and/or require large quantities of an alkalizing agent to restore the pH, which increases salinity.

The formation of the coagulating species ($Al(OH)_3$) from the dissolution of aluminium plates can be described by the following reactions [21-23]:

At the anode:

$$2Al \rightarrow 2Al^{3+} + 6e^- \quad (1)$$

At the cathode:

$$6H_2O + 6e^- \rightarrow 3H_2 + 6\,OH^- \quad (2)$$

In the bulk solution:

$$Al^{3+} + 3H_2O \rightarrow Al(OH)_3 + 3H^+ \quad (3)$$

The formation of poly-hydroxides such as $Al(H_2O)^{3+}$ and $Al_6(OH)_{15}^{3+}$ are also possible [14, 24, 25].

EC has been used for the treatment of groundwater from contaminants such as arsenic [26], nitrates [18, 27], chromium [28], petroleum [29], humic acids [30], and perfluoroalkyl substances [31]. Most studies on EC have focused on water quality [32-36]. However, there is relatively few studies on how changes on the electrode surface may impact the EC process. EC is not always efficient in purifying water in terms of energy costs [37]. Several factors such as current density, flow rate, plate spacing, and electrode and solution composition may affect the effectiveness of contaminant removal and energy consumption [38, 39]. Passivation of aluminium electrodes, as well as high solution resistance may result in excessive energy requirements [40-42]. The presence of pitting promoters is also important to allow de-passivation of aluminium. Martin et al. compared passivation of pure aluminium and Al 1050 with a rough or smooth surface in neutral electrolyte solutions - the rough surface experienced "spontaneous de-passivation" even without the addition of pitting promoters such as chloride [43].

In this study, Al plates were used as the sacrificial electrode (anode) and cathode in an EC process for the treatment of synthetic groundwater. The EC cell was operated as a continuous-flow reactor with a short hydraulic retention time (HRT). Changes on the aluminium electrode surface were characterized over time using a suite of physical, chemical, and electrochemical tools, and the resulting changes in water quality are discussed.

Material and Methods

Materials:

Electrochemical measurements, EC experiments and grazing incidence X-ray diffraction (GI-XRD) were performed using 0.254 cm thick 5052 Aluminium (96.8% Al, 2.47% Mg, 0.25% Fe, 0.13% Si, 0.2% Cr, 0.056% Mn, 0.023% Ti, 0.019% Cu, 0.018% V, 0.013% Zn, 0.01% Ga, 0.007% Ni) provided by WaterTectonics (Everett, WA). SEM, TEM, SAI and XPS were performed with 0.081 cm thick 5052 Aluminium purchased from McMaster-Car (Chicago, IL). $MgCl_2 \cdot 6H_2O$, $CaCl_2 \cdot 2H_2O$, $NaSiO_4 \cdot 5H_2O$ and 37% HCl were purchased from Acros Organics (Waltham, MA) and used without further modification. $NaHCO_3$ and 200 proof ethanol were purchased from Fisher Chemical (Waltham, MA) and used without further modification.

Methods:

Synthetic Groundwater

Synthetic groundwater was formulated based on the water quality characteristics of groundwater from the City of Longville, Washington, kindly provided by WaterTectonics. The composition of the synthetic groundwater is listed in Table 1. The pH of the resultant solution was pH 8.6.

Table 1: Synthetic Groundwater content

Chemical	Concentration (mM)
Na_2SiO_3	0.85
$NaHCO_3$	2.2
HCl	1.4
$CaCl_2$	0.676
$MgCl_2$	0.272

Electrocoagulation process

A flow-by EC cell containing two electrodes spaced 0.32 cm apart (Figure 1) was used in all experiments. Synthetic groundwater was pumped at 3 different flow rates (0.5, 1 and 1.46 litres per minute (LPM)), corresponding to an HRT of 2.1, 1.06, and 0.73 seconds, respectively, and a velocity of 7.2, 14, and 21 cm/s, respectively. The synthetic groundwater was pumped using a peristaltic pump (Cole Parmer, IL, USA). Prior to the EC experiments, the aluminium electrodes were polished with 150 grit sandpaper, degreased with ethanol and flushed with DI water. The total exposed area of the anode and cathode was 55.6 cm^2 each. A DC power supply (Siglent Technologies SPD3303X, MN, USA) capable of supplying up to 3.2 A and 60 V of power was connected to the electrodes. The output voltages were logged into a computer using a self-written code (Python 3.0.3) at different current densities (2, 10 and 25 mA/cm^2). Water samples were collected every 5 min into a 50 mL centrifuge tube (Falcon, Corning Life Sciences, MA, USA) until 20 L of synthetic groundwater passed through the system. pH, conductivity, turbidity, silica, and hardness levels were measured from the collected water samples after a settling time of 24 h.

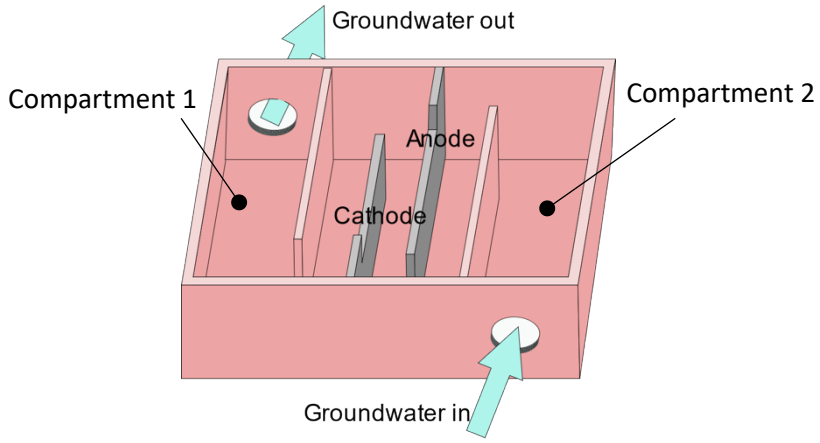

Figure 1: Flow through EC cell design used for the experiments in this study.

Electrochemical measurements

Electrochemical measurements were conducted using a potentiostat (CHInstruments, CHI6005E) with a 3-electrode setup. Both working and counter electrodes were the aluminium plates, and the reference electrode was a Ag/AgCl electrode in 3 M KCl and saturated AgCl,

which was placed in either compartment 1 or 2 (Figure 1). To achieve the high current densities needed to drive the EC process using the potentiostat, the working electrode was masked so that only 2 cm^2 were exposed to the solution, which allowed us to maintain identical flow conditions during EC experiments and electrochemical characterization steps while achieving current densities as high as 25 mA/cm^2; during these electrochemical characterization experiments, the counter electrode surface area was kept at 55.6 cm^2. The electrodes were masked using vinyl tape (Scotch, Super 33+, MN, USA). Electrochemical measurements were performed in the flow-by EC reactor (Figure 1), with the reference electrode placed in compartment 1 when electrochemical measurements were made to the anode, and in compartment 2 when electrochemical measurements were made on the cathode. The reference electrode was not placed between the anode and cathode, so as not to disrupt the feed flow as it passed along the electrodes. Electrochemical measurements were performed at both open circuit potential (OCP) and during the application of higher voltages needed to drive the EC process.

Electrochemical Impedance Spectroscopy (EIS) was conducted using an AC amplitude of 5 mV in the frequency range from 1MHz to 0.1 Hz, with 12 points collected per decade. EIS curves were modelled and fitted using CHI software. Tafel plots were obtained using a scan rate of 1 mV/s in the anodic direction.

To evaluate the impact of mass transfer of dissolved aluminum on the electrochemical properties of the electrode surface, EIS experiments were conducted using a rotating disc electrode (RDE) (Pine Research, NC, USA). The RDE had a diameter of 5 mm and was made of 5052 aluminium alloy, polished to mirror finish, and fitted to Pine Research Modulated Speed Rotator (Pine Research, NC, USA). The RDE was placed in the flow-by cell used in the EC experiments. An aluminium 5052 alloy plate with 56 cm^2 surface area was used as the counter electrode, and a Ag/AgCl electrode was used as the reference electrode.

Surface and Water Characterization

Solution pH was measured using a portable pH meter (Thermo Scientific, Orion 720A, MA, USA), and turbidity was measured using a turbidity meter (Hach, 2100P, CO, USA). Effluent concentrations of Al, Si, Mg and Ca were measured using inductively coupled plasma-mass spectroscopy (ICP-MS, PerkinElmer, NexION 2000, MA, USA). Constituent removal efficiency was calculated using the following equation:

$$Removal\ efficiency\ (\%) = \frac{C_o - C_f}{C_o} * 100 \quad (4)$$

Where C_o is the initial concentration of constituent and C_f is the supernatant concentration of the constituent after EC and 24 hours of settling.

The chemical composition of the electrode surface was determined using X-ray photon spectroscopy (XPS) (Kratos Axis Ultra DLD spectrometer equipped with a monochromatic Al Kα X-ray source, Manchester, UK). High-resolution spectra were calibrated using carbon tape (Ted Pella, CA, USA) with a known C1s binding energy of 284.6 eV. Raw data were processed using CasaXPS software (version 2.3.19). The electrode surface was characterized using scanning electron microscopy (SEM ZEISS, Supra 40VP, Oberkochen, Germany) equipped with an energy-dispersive X-ray detector (EDAX). Cross sections of the electrode were obtained using ion beam etching and viewed by transmission electron microscopy (TEM, FEI

Titan S/TEM, MA, USA). The electrode surface area index was obtained using an optical profiler (Bruker NT9300, MA, USA). Grazing incidence X-ray diffraction (GI-XRD) patterns were obtained by X-ray diffractometer (PANalytical, Malvern UK) with Cu kα radiation at a scan rate of 4°/min. The X-rays were impinged on the sample with an incident angle of 1°.

Model to predict pH at the cathode surface and solution shear rate in between the anode and the cathode

The pH on the electrode surface was simulated using COMSOL Multiphysics©. The electrodes were modelled as planar electrodes that generate Al^{3+} ions at the anode given by equation (1) , and OH^- ions through water electrolysis at the cathode given by equation (3). The flux of each ionic species was calculated from the current density using Faraday's equation:

$$J_x = \frac{i}{zF} \quad (5)$$

Where i is the current density, z is the charge of the ionic species, and F is the Faraday constant. Diffusion of OH^- and Al^{3+} are assumed to be governed only by Fick's 1st law:

$$J_x = -D_x \nabla C_x \quad (6)$$

D_x is the diffusion coefficients of OH^- and Al^{3+}, taken to be 5.27e-9 and 1.2e-9 m^2/s respectively [44, 45]. C_x is the concentration of each species. pH at the electrode surface was simulated under laminar flow conditions. No-slip boundary conditions were assumed at the electrode/water interface. The volume between the two electrodes was modelled as a rectangular section. The mesh-size was user-controlled with selection of the mesh size based on a sensitivity analysis, which showed that the average OH^- concentration and solution shear rate perpendicular to the flow direction was not significantly impacted by the selected mesh size (Figure S1). In addition, the impact of gas evolution (H_2) was ignored during this modelling.

Results and Discussion

Electrocoagulation

EC was conducted in a cell as depicted in Figure 1 at different flow rates and current densities; pH, conductivity, turbidity, silica, and hardness removal were determined over time after a settling time of 24 h and are shown in Figure S2. Both hardness and silica removal rates improved with increasing current densities and decreasing flow rates (Figure S2(a-f)). Hardness removal ranged from 0 % to 11 ± 1 %, and silica removal ranged from 0 % to 50 ± 4 %. This was a result of increasing total aluminium concentrations caused by higher corrosion rates paired with lower flow rates (resulting in lower shear rates (Figure S3)), which enabled the formation of a larger amount of floc for contaminant removal. Removal rates and EC performance were stable at all time points sampled for all current densities and flow rates, showing a constant solution chemistry after the first 5 minutes for each experiment.

The total concentration of dissolved aluminium (measured using ICP-MS) as a function of the charge loading (C/L) is shown in Figure 2(a). Here, charge loading is defined as the Coulombs of charge applied to the electrode per litre of synthetic groundwater passed through the EC cell, given by:

$$Charge\ loading = \frac{I * t}{V} \quad (7)$$

where I is current, t is the retention time, and V is the volume of water passed between the electrodes within the retention time.

The measured concentration of aluminium in the solution was compared to the theoretical concentration of aluminium expected to be dissolved as a function of the current passed through the electrodes, estimated using Faraday's law of electrolysis [46]:

$$Theoretical\ Al\ concentration = \frac{I * t}{F * Z * V} \quad (8)$$

Where F is the Avogadro number and Z is the aluminium ion charge.

It was found that the experimental aluminium concentration measured by ICP-MS was higher than the theoretical Al concentration, with the difference between the observed and predicted Al concentrations increasing at higher charge loadings (Figure 2(a)). The % difference between the theoretical aluminium concentration and the total aluminium concentration was calculated using the following equation:

$$\%\ \text{difference} = {(\text{Total Al conc} - \text{Theoretical Al conc})}/{\text{Theoretical Al conc}} \quad (9)$$

This difference reached a maximum at 57 C/L, decreasing somewhat at higher charge loading. We attribute the higher measured aluminium concentrations to locally elevated hydroxide concentrations at the cathode/water interface, which cause the aluminium cathode to corrode and release aluminium into the water [47-49]. At high pH values (pH > 8), aluminium ions exist predominantly in the form of $Al(OH)_4^-$ [50, 51]. At around pH 6 to 8 is where aluminium precipitates ($Al(OH)_3$) prevails [52]. pH conditions are readily achieved at the electrode/water interface under high current densities, which can lead to the dissolution of Al from the cathode surface. pH at the cathode surface for the different flow rates and current densities were simulated using COMSOL and are given in Figure 2(b). The model predicted that the pH at the cathode surface ranges between pH 12.2 to pH 13.4, depending on flow rates and current densities, with higher densities and lower flow rates leading to overall higher pH along the electrode surface. There is a sharp drop in pH as one moves away from the cathode surface towards the bulk, but under all conditions modelled, the local pH up to 100 μm away from the electrode was over 11. Such high pH conditions can readily lead to the dissolution of Al from the cathode surface. The impact of dissolved aluminum ions on the local pH is not captured in the model. However, the diffusion of aluminium ions towards the cathode beyond 1.175 mm from the anode surface (or 2 mm from the cathode surface) is negligible as illustrated in Figure S4.

Hydrogen evolution at the cathode can lead to the formation of aluminium hydrides (AlH^{3+} and AlH^{2+}), which could contribute to Al dissolution [53]. Aluminium corrosion in alkaline media begins from the formation of an aluminium hydroxide film, followed by the incorporation of hydroxide ions into the film and migration towards the aluminium/film interface [47]. The aluminium hydroxide film is then chemically attacked by hydroxide ions to form soluble aluminate ($Al(OH)_4^-$) according to the following reactions:

$$Al + 3OH^- \rightarrow Al(OH)_3 \quad (10)$$

$$Al(OH)_3 + OH^- \rightarrow Al(OH)_4^- \quad (11)$$

Based on the above chemical reactions, the aluminium dissolution rate at the cathode will depend on the concentrations of $Al(OH)_4^-$ and OH^- ions. As the transport limit of $Al(OH)_4^-$ ions is reached at the electrode/water interface, less Al can be hydrolysed into the solution and the % difference between predicted and observed Al concentrations becomes increasingly dominated by the Al dissolution at the anode, and the % difference decreases.

Contrary to some studies, solution pH did not increase as EC proceeds [51, 54] Figure 2(c)); changes in the pH at the different flow rates are shown in Figure S5. This could be due to differences in both the water chemistry and retention times. While water splitting at the cathode produces alkalinity, aluminium combines with these ions to lower the solution pH. It is unclear why a pH change was not observed in this study.

The concentration of Al measured in the supernatant after a 24 h settling period was measured as a function of the charge loading (Figure 2(a)). At low charge loading (30 C/L), the concentration of Al in the supernatant was nearly identical to the theoretical and total measured concentrations of Al coming out of the reactor, indicating that at these low charge loadings little floc was formed. Incidentally, this correlates well with the observed Si and hardness removal, and turbidity at low current densities (all flow rates with 2 mA/cm^2) and high shear rates, which showed low removal and at the same time higher turbidity, emphasizing the importance of floc formation for water quality enhancement (Figure 2(d)-(f)). Importantly, the concentration of Al in the supernatant plateaued, and actually somewhat declined, with increasing charge loading (while total Al concentrations increased), indicating that Al floc was formed and settled out at higher charge loadings. As the current density increased, the total Al concentration increased, and as a result, silica and hardness removal improved. Silica reached the highest removal efficiency of $50 \pm 4\%$ and hardness removal reached 11 ± 1 % at the highest charge loading investigated in this study (167 C/L). It is important to note that these removal levels were achieved at very low residence times (< 2.1 seconds).

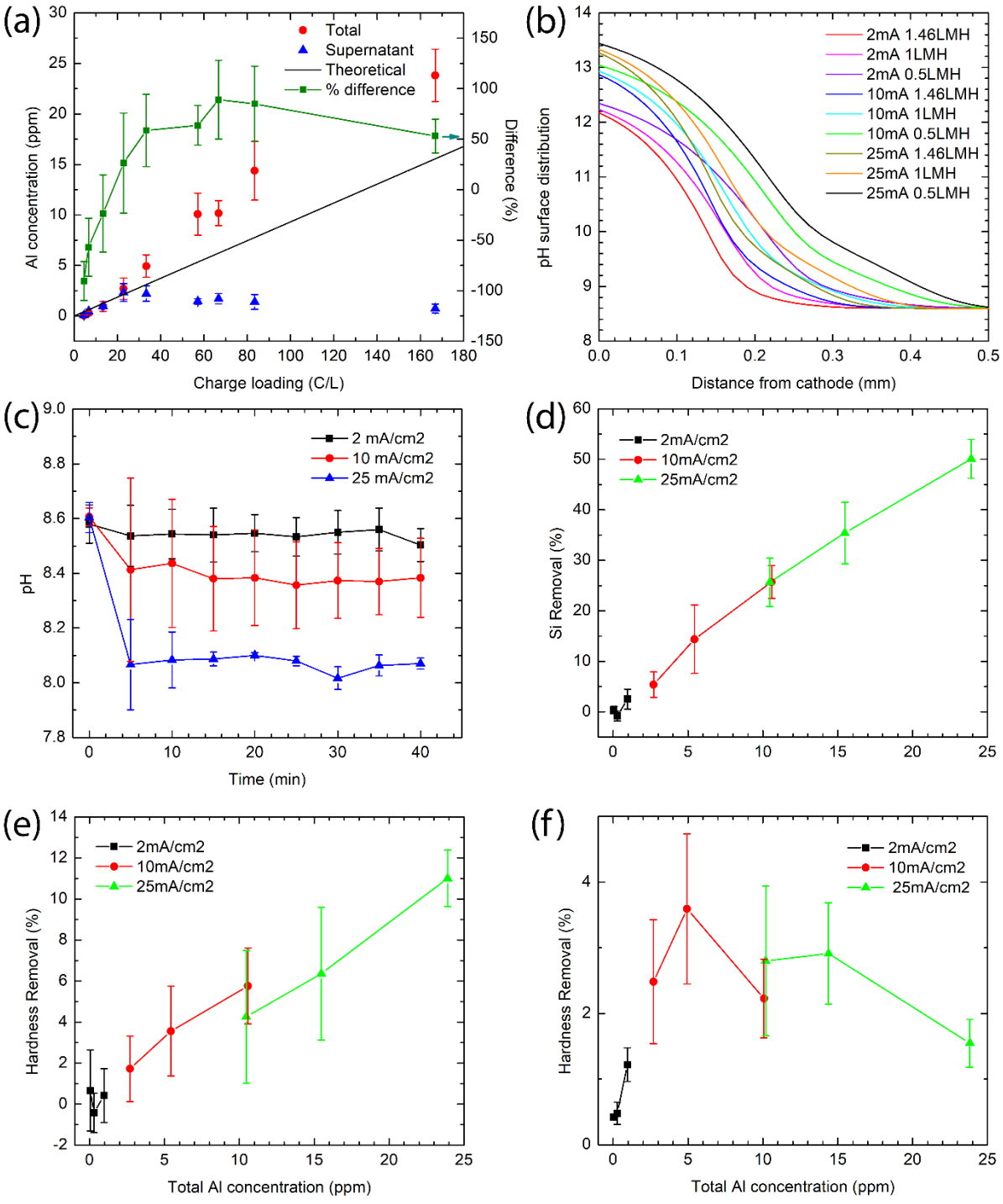

Figure 2: (a) Aluminium concentration in treated synthetic groundwater measured by ICP-OES plotted against charge loading for total dissolved aluminium, supernatant aluminium and theoretical aluminium concentrations. (b) COMSOL simulated pH profile as a function of distance from surface of the cathode. (c) Change in pH of synthetic groundwater as it passes through the EC cell. (d) Silicon and (e) hardness removal (%) from synthetic groundwater supernatant measured by ICP-OES plotted against charge loading. (f) Turbidity of synthetic groundwater supernatant after 24 h settling time.

300

Electrode characterization

The voltage necessary to drive the EC process at flow rates of 0.5, 1 and 1.46 LPM, and current densities of 2, 10 and 25 mA/cm^2 were recorded (Figure S6). The stable voltage at the different current densities indicates that minimal electrode cathode scaling (e.g., $Mg(OH)_2$, $CaCO_3$) occurred, since mineral scale creates an electrically insulating layer that would require higher potentials to maintain a given current density. It was also observed that at a flow rate of 0.5 LPM, a higher voltage was necessary to maintain the different current densities (2 and 10 mA/cm^2) compared to 1 and 1.46 LPM. This shows that redox reactions at the electrodes at a low flow rate (0.5 LPM) and lower current densities (2 and 10 mA/cm^2) were transport-limited, while at higher flow rates (1 and 1.46 LPM) and high current density (25 mA/cm^2), the reaction was diffusion-limited. This was further supported by the fact that the necessary voltage to drive 2 and 10 mA/cm^2 was similar at the higher flow rates of 1 and 1.46 LPM.

As the EC process proceeds, Al dissolves from the surface of the anode and cathode, while the concentration of other elements change due to mineral deposition/growth and/or impurities in the electrode alloy itself. XPS was performed on the electrode surfaces used in the experiments at the different current densities and 0.5 LPM to determine changes to the their surface chemical composition, with the data plotted as a ratio between the % atomic composition of a given element to the % atomic composition of aluminium (Figure 3(a) and Figure 3(b)). The original atomic % of the elements are displayed in Figure S7. On both the anode and cathode, at all current densities, the ratio between oxygen and aluminium increases after EC indicating the presence of a thicker layer of aluminium oxide, or the formation of metal oxide/hydroxide scale. A small amount of magnesium and calcium detected on the anode were likely part of the aluminium 5052 alloy content and impurities [55]. At the cathode, the calcium and magnesium ratio increased after EC, suggesting the formation of scalants (e.g., $Mg(OH)_2$, $CaCO_3$). There was no trend in the change of scalant to aluminium ratio relative to the different current densities. No clear trend was obvious in cathode scaling. Cathodes that participated in the EC at 2 mA/cm^2 had the highest scalant to aluminium ratio, followed by 25 mA/cm^2 and then 10 mA/cm^2. The differences in scalant to aluminium ratio could be the effect of both a balance between scalant formation and aluminium shedding at high pH, and scale removal from evolved H_2.[56]

In cross-sectional TEM images of a fresh Al electrode, an anode, and as a cathode after EC at 25 mA/cm^2 for 40 min, a second aluminium phase, likely Al oxide, was observed (Figure 3(c)-(e)). For fresh Al, the Al oxide thickness was only 3.5 ± 0.5 nm. However, after EC, the Al oxide phase thickness increased to 7 ± 1 nm on the anode, which is consistent with the XPS results showing an increase in the O/Al ratio on the anode after EC. In contrast, the aluminium oxide layer on the cathode did not exhibit a clear metal/metal-oxide interface like that of a fresh piece of Al or the anode and had an average thickness of 5 ± 2 nm. This could be caused by different dissolution mechanisms and reductive conditions at the cathode. While Al was electrochemically dissolved at the anode with a high concentration of oxygen, Al dissolution from the cathode was purely chemical in nature, i.e., driven by hydrolysis (Equations 2 and 3).

Figure 3(f)-(h) show SEM images of a fresh Al electrode, the anode, and cathode surfaces after EC at 25 mA/cm^2 for 40 min, respectively. On the anode, crystalline square pits were observed across the entire surface, a result of Al dissolving at certain facets of the aluminium lattice (Figure 3(g)) [57]. At the cathode, some mineral scale was observed together with some

circular pits (Figure 3(h)). The coverage of the mineral scale increases with current density, where coverage was the highest at 25 mA/cm^2 followed by 10 mA/cm^2 and 2 mA/cm^2 (Figure S10). The shallow circular pits were observed on cathodes subjected to 10 and 25 mA/cm^2. The pits are formed due to the locally high pH at the cathode/water interface, which leads to aluminium dissolution [58, 59]. Importantly, these pits were observed on the Al cathodes even in the absence of chloride (when the background electrolyte was only a Na_2SO_4 solution, i.e., a solution with no pitting agent), in which case the anode did not experience significant corrosion (Figure S11(a)), strengthening the claim that cathodic dissolution does occur on aluminium surface as a result of the elevated local pH (Figure S11(b))

Figure S12 shows the surface area index (SAI) (defined as the total surface area divided by the area of a completely flat surface) of the electrodes after EC at different current densities for 40 min, measured using an optical profiler. The SAI of the cathode remained relatively constant at the different current densities, indicating no significant change in its effective surface area regardless of the applied current densities. While mineral scaling is expected to increase surface roughness (and hence, the SAI) on the cathode, the relatively soft water, and mild scaling observed in the SEM images, may be responsible for the lack of change in cathode SAI values. However, in hard water conditions, where cathode scaling can be extensive, the SAI vaues could be significantly larger. In contrast, the SAI of the anode increases from 1.7 ± 0.4 before corrosion, to 5.9 ± 0.4 as EC proceeds at higher current densities but does not change much if it is raised above 10 mA/cm^2. Plateauing of the SAI above 10 mA/cm^2 is likely because of complete corrosion of the anode surface and similar corrosion pattern, where a certain aluminium crystal facet was preferentially dissolved (Figure 3g and Figure S13). An increase in the effective surface area of the electrode would mean a lower effective current density necessary to produce the same current during EC. According to Ohm's law, if the resistance remains the same, a smaller voltage would be required to drive a smaller current density [60].

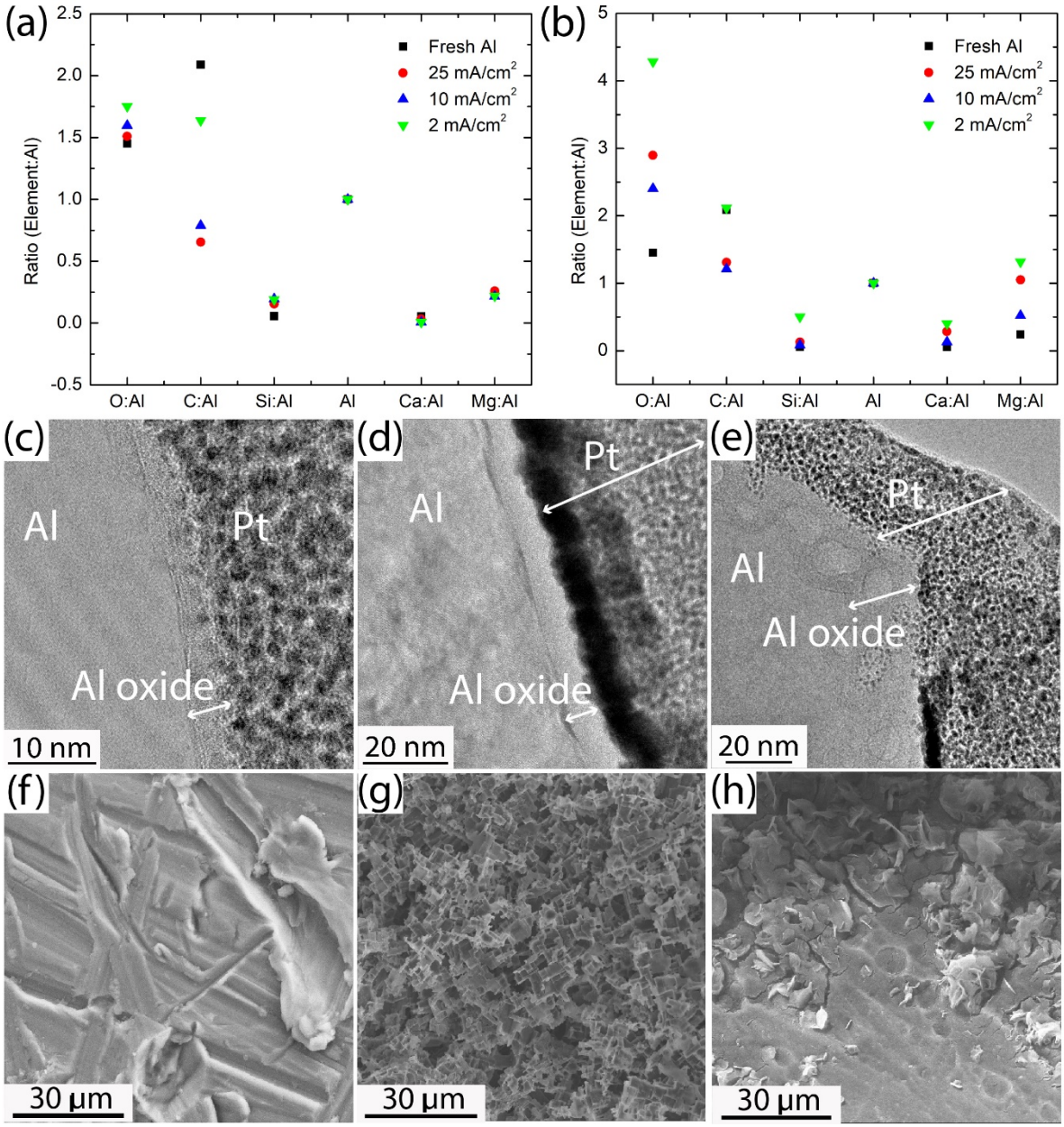

Figure 3: XPS (a) anode and (b) cathode surface atomic composition normalized against Al atomic composition. Cross-sectional TEM images of (c) fresh aluminium electrode, (d) Al anode and (e) cathode after EC at 25 mA/cm² for 40 min. SEM surface characterization of (f) fresh aluminiuml electrode, (g) aluminium anode and (h) cathode after EC at 25 mA/cm² for 40 min.

Electrochemical characterization during EC

High-voltage EIS measurements and Tafel plots were obtained by masking the anode or cathode to reduce their effective surface area and achieve the needed current densities with the potentiostat. Importantly, the working electrode of the potentiostat (either anode or cathode) was masked (active surface area of 2 cm^2), while the counter electrode was unmasked and had a larger surface area (55.6 cm^2). The cell potential was supplied and monitored throughout the experiments using an external power supply where the current density of the working electrode was set to 15 mA/cm^2 in synthetic groundwater and also in 3 mM Na_2SO_4 solution (Figure 4(a)

and (b)). At 10, 20, 30 and 60 min time intervals, the power supply was disconnected, and the potentiostat was connected to obtain the EIS measurements and Tafel plots.

When the anode was used as the working electrode (anode-controlled), the cell potential remained comparatively stable at approximately 7.3 V. From the SAI values (Figure S12), we know that the effective surface area of the anode increases after the application of a corroding potential. The increase in effective surface area would lower the potential necessary to drive a specific current. However, although the effective surface area of the anode increased, the effects were counteracted by an increase in the oxide layer thickness from 3.5 ± 0.5 nm (fresh aluminium) to 7 ± 1 nm (after EC) at the anode as shown by the TEM images in Fig 3(c),(d). Because of the balance between a resistance reducing (increase in SAI) and a resistance increasing (increase in oxide layer thickness) changes on the anode, the potential needed to drive the same current throughout the experiment remained relatively unchanged.

In contrast to the anode-controlled experiment, the total cell potential required in the cathode-controlled (i.e., the cathode used as the working electrode) experiment dropped as the experiment proceeded, which was unexpected. Since the oxide layer thickness increased (from 3.5 ± 0.5 nm on a fresh electrode to 5 ± 2 nm after EC at the cathode (Figure 4e)) and since mineral scale formed on the cathode, it was expected that the resistance to charge transfer would increase, leading to higher potentials needed to provide the constant current. Water electrolysis at the cathode forms hydroxide ions that can thin the aluminium oxide layer through dissolution, or increasingly hydrate it through the formation of gibbsite or boehmite [61]. Although an increase in local pH did not cause thinning of the oxide layer, we speculate the oxide layer was in the form of gibbsite or boehmite. The hydrated form of aluminium oxide (gibbsite and boehmite) has been shown to be more electrically conducting than crystallized aluminium oxide [62], possibly explaining the decrease in the cell potential required at the cathode over time. GI-XRD results confirm the existence of Gibbsite on the surface of the cathode (Figure 5c). The GI-XRD spectrum of a fresh aluminium electrode as well as the anode after EC at 25 mA/cm^2 for 40 min show peaks at $2\theta = 38.3°$ belonging to γ-Al_2O_3, and $2\theta = 44.5°$ and 64.9° belonging to aluminium [63-65]. At the cathode, additional peaks belonging to Gibbsite were detected at 17.8° and 20.2° [66, 67], confirming a change in the aluminium oxide crystal structure at the cathode. These peaks were not detected in the mineral scale collected from the cathode surface, further showing the structural change occurring in the aluminium oxide top layer of the cathode surface. The scalants show aluminium peaks at 38.3°, 44.5° and 64.9°, consistent with aluminium floc. Other peaks, possibly belonging to calcium and magnesium salts, were also detected on the cathode surface and scalants removed from the cathode surface. It was shown that the most energy consuming electrode in the EC of synthetic groundwater was not the cathode (supposedly caused by scaling and bubble formation), but rather the anode due to constant surface properties in such a set-up

To explore aluminium dissolution in a chloride-free environment, Na_2SO_4 with the same ionic strength as the synthetic groundwater (3 mM) was used to conduct EC under the same conditions (Figure 4(b)). However, to achieve a current density of 15 mA/cm^2 in the anode-controlled experiment, a cell potential of more than 40 V was necessary, which was 5 times higher than in synthetic groundwater (i.e., in the presence of Cl). Further inspection of the aluminium anode surface by SEM after EC revealed little to no dissolution of the electrode (Figure S10(a)). It is likely that the application of anodic potentials in the Na_2SO_4 solution only caused the migration of oxygen ions through the aluminium oxide layer, leading to a thickening

of this electrically insulating layer, which increased the resistance to charge transfer [68]. In contrast, the presence of chloride leads to pitting and aluminum dissolution, allowing for surface renewal and lower cell potentials.

In the cathode-controlled experiment in Na_2SO_4, the cell potential required to maintain a constant current remained steady, unlike synthetic groundwater where the cell potential decreased. TEM images of the cathode after EC in Na_2SO_4 and in groundwater were very different (Figure S14 a,b). Instead of having circular oxide structures that extend deep into the aluminium, the oxide layer was flat, similar to that observed on fresh aluminium and the anode. A TEM-EDS image shows a 2nd phase near the surface of the Al electrode composed primarily of aluminium and oxygen (Figure S13c-f). The difference in structure of the aluminium oxide layer could be caused by a difference in the mechanism of aluminium dissolution at the cathode in chloride-containing and chloride-free solutions. While aluminium dissolution at the cathode is mainly caused by hydrolysis in chloride-free solutions, dissolution in chloride-containing solution is partly caused by the penetration of chloride ions and formation of soluble aluminium chloride complexes.

Tafel plots were obtained for the electrodes at different time intervals under 15 mA/cm^2 anode- and cathode-controlled EC experiments in synthetic groundwater after 60 minutes of operation (Figure 4(d) and Figure 4(e)). Over time, the corrosion potential (E_{corr}) moved to more negative values in the anode-controlled experiment (-0.6 to -0.71 V), indicating a loss in passivity [69]. This loss in passivity could be caused by pH changes at the anode as Al^{3+} ions take up hydroxide ions to create a low pH environment [70]. At the cathode, the shift of E_{corr} was more pronounced (-0.6 to -1.3 V), which could also indicate a change in local pH [71]. In both cases, once the EC reaction begins, the corrosion current increases, indicating a weakened protective film around the aluminium electrodes [72].

EIS was conducted throughout the experiments in synthetic groundwater at different time intervals (0, 10, 20, 30 and 60 min) at the voltage needed to achieve 15 mA/cm^2. Nyquist plots show a single semi-circle that has a relatively constant value (Figure 4f)). A Randle's circuit was used to fit the EIS data, with Rs being the electrolyte resistance, R1 being the charge transfer resistance and CPE1 being a constant phase element. On the anode, R1 did not change over time (staying at approximately 190 Ω). In contrast, R1 of the cathode decreased over time, from 180 Ω to 120 Ω over 60 min (Figure 4(g)). This is likely caused by a combination of an increase in surface area due to pit formation by chloride and hydroxide attack, and the formation of an increasingly electrically conductive aluminium hydroxide layer at the cathode. The constant anode R1 and the decreasing cathode R1 are in-line with the observed changes in the cell potential shown in Figure 4(a).

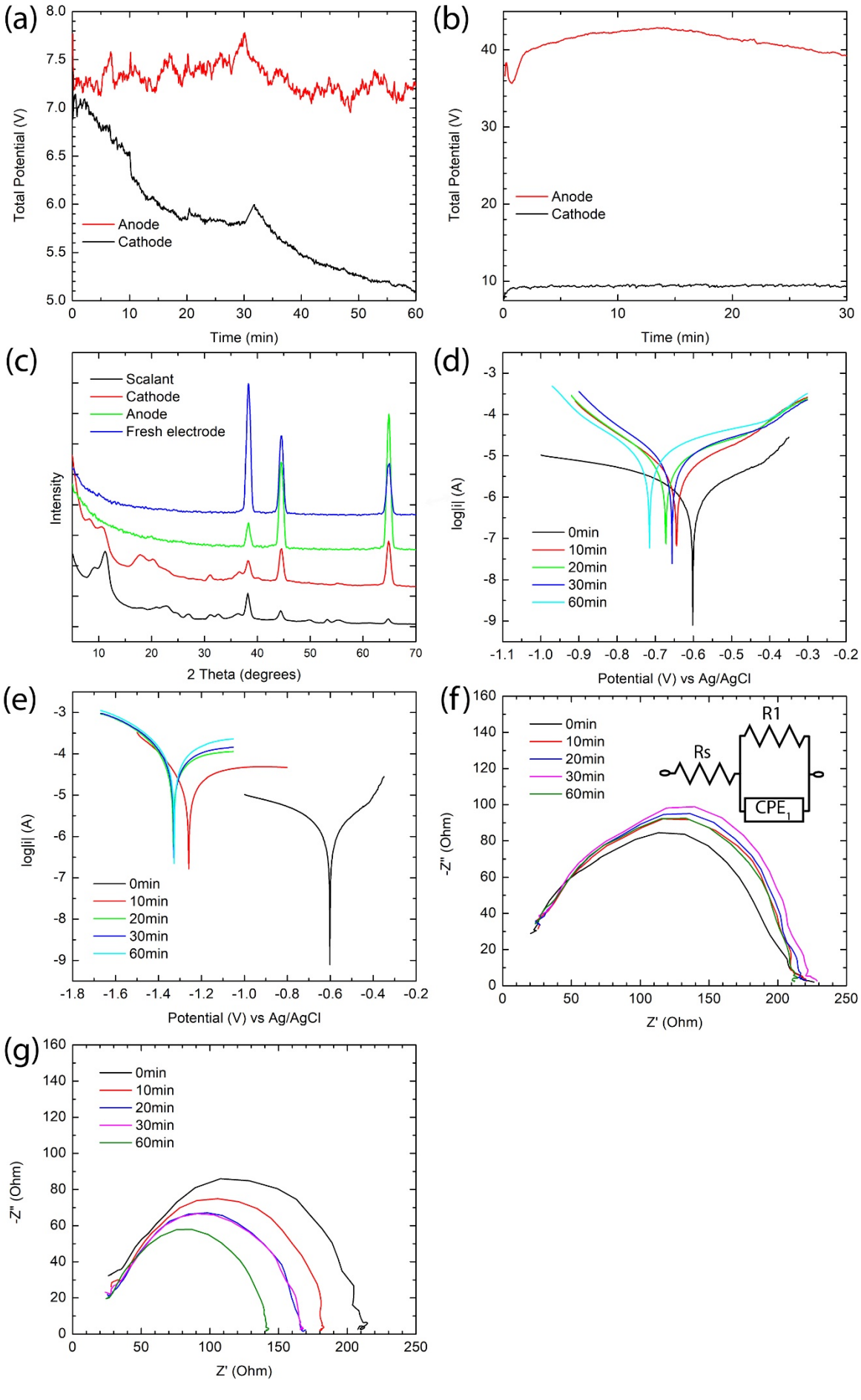
(a)
Total Potential (V)
Time (min)
Anode
Cathode
(b)
Total Potential (V)
Time (min)
Anode
Cathode
(c)
Intensity
2 Theta (degrees)
Scalant
Cathode
Anode
Fresh electrode
(d)
log|i| (A)
Potential (V) vs Ag/AgCl
0min
10min
20min
30min
60min
(e)
log|i| (A)
Potential (V) vs Ag/AgCl
0min
10min
20min
30min
60min
(f)
-Z'' (Ohm)
Z' (Ohm)
0min
10min
20min
30min
60min
R1
Rs
CPE1
(g)
-Z'' (Ohm)
Z' (Ohm)
0min
10min
20min
30min
60min

Figure 4: Overpotential changes in the electrodes in (a) 3 mM Na_2SO_4 and (b) synthetic groundwater. (c) GI-XRD data of the fresh aluminium electrode, cathode and anode after EC at 25 mA/cm^2 for 40 minutes in synthetic groundwater, and scalants collected from the surface of the cathode. Tafel plots of the (d) anode-controlled and (e) cathode-controlled experiments in synthetic groundwater over increasing time at 15 mA/cm^2. EIS of the (f) anode-controlled and (g) cathode-controlled experiments in synthetic groundwater over increasing time at 15 mA/cm^2.

EIS at different current densities

To further explore changes on the electrode surface during EC, EIS was conducted at different voltages to achieve a range of current densities from 0 to 15 mA/cm^2, with Nyquist plots obtained at the anode and cathode (Figure 5(a) and Figure 5(b)). The experiments were conducted starting from high current densities to OCP (15 mA/cm^2 to 0 mA/cm^2) so that surface area changes between the different current densities would be kept to a minimum. It was observed that at lower current densities, 2 semi-circles can be seen at both the electrodes. However, with increasing current densities, the semi-circle that appears at low frequencies diminished in size and eventually disappeared above 2 mA/cm^2.

To determine the cause of the low-frequency semicircle, EIS was conducted using a rotating disc electrode (RDE) at OCP. The RDE rotates at high speeds during experiments to minimize mass-transfer limitations at the electrode/water interface. As the rotation speed increases, the thickness of the diffusion boundary layer changes and can be approximated by the following equations [73, 74]:

$$\delta = 1.61\sqrt[3]{D_o}\frac{\sqrt[6]{v}}{\sqrt[2]{\omega}} \quad (124)$$

$$\omega = 2\pi(rpm)/60 \quad (13)$$

Where δ is the diffusion layer thickness, D_o is the diffusion coefficient, v is the kinematic viscosity, ω is the angular rotation rate, and rpm is rotations per minute.

Rotation speeds were adjusted from 100 rpm to 2000 rpm, corresponding to δ values between 6.8 – 1.5 μm for Al^{3+}, assuming the diffusion coefficient of Al^{3+} in solution is 1.2 x 10^{-9} m^2/s [45]. Figure 5(c) shows Nyquist plots conducted at OCP at 4 different rotation speeds. There were no apparent changes in the semi-circles at both high and low frequencies, indicating that that both the high and low frequency semi-circles are not affected by the diffusion of Al^{3+} ions through the different thicknesses of the diffusion layer generated in this study. Thus, we attribute the high-frequency semi-circle observed in the Nyquist plots to charge transfer resistance (R1), and the low-frequency semi-circle to the electrical resistance of the Al oxide layer of the electrode (Rd). Figure 5(d) shows the equivalent circuit model used to describe the EIS results at both high voltage and at OCP. At high voltages (-2.45 V to -8 V at the cathode, and 0.6 V to 5V at the anode) a simple Randles circuit that consists of the electrolyte resistance (Rs), R1 and a constant phase element (CPE_1) is used since only one semi-circle was observed [75]. At OCP, the Randles circuit is modified to include another resistor (Rd) and constant phase element (CPE_d) placed in parallel to model the second observed semi-circle at low frequency.

EIS was also conducted at 15 mA/cm^2 at different rotation speeds. There was only 1 semi-circle in the high frequency region and no obvious change in R1 at the different rotation speeds

(Figure 5(e)). Based on this observation, it is likely that diffusion of Al^{3+} ions away from the electrode surface is not a limiting factor to the aluminium dissolution rate in the conditions tested in this study. Even without the use of the RDE, we speculate that the continual movement of synthetic groundwater in the flow-by EC cell helped to reduce concentration polarization along the aluminium anode surface that prevented the formation of a thick diffusion boundary layer caused by saturation of Al^{3+} ions.

The disappearance of Rd at high current densities can be explained by the provision of an electric field that polarizes the electrically insulating Al oxide layer of the electrode to the point of dielectric breakdown, and allow current flow across the Al oxide layer [21, 68, 76].

From the EIS measurements conducted at different voltages at both the cathode and the anode, it was determined that as the current density increased, R1 continues to decrease in magnitude (from 230 ± 15 Ω at OCP to 164 ± 4 Ω at 15 mA/cm^2) (Figure 5(a) and Figure 5(b)). The decrease in R1 with increasing potentials is similar to the non-linear relationship between current and overpotential observed by Tafel [77], which is:

$$\eta = a + b\log i \qquad (14)$$

Where η is the overpotential, i is current, and a and b are constants. The exponential relationship between η and i results in R1 (given by η/I) decreasing as the current density increases. An explanation for the drop in R1 is that as the electrode potential is increased in the negative or positive direction, the energy level of electrons/holes in the electrode increase to a point that permits them to transfer from the electrode to the electrolyte [78]. As the electrode potential increases, a larger percentage of electrons/holes [79], not necessarily linear to the applied potential, are raised to the electron transfer energy level.

Figure 5(f) shows changes in R1 values as the electrodes are polarized at increasing and then decreasing current densities. Starting from high current densities, R1 values increase as the current density decreases from left to right. However, when the current density increases again, R1 values decrease to values lower than their original point. This hysteresis could result from an increasing effective surface area at the anode, and an increasingly electrically conducting aluminium oxide layer at the cathode. When the EIS was first measured at 15 mA/cm^2 at the anode, the fresh surface of the aluminium electrode had not corroded yet. As the electrode was continually polarized to conduct EIS measurements at high current densities, the electrode surface corroded, resulting in a growing anode surface area. A larger anode surface would mean the effective current density applied to the anode was lower the second time the same current was applied. Thus, a lower overpotential was required, resulting in a drop in R1 (given by η/i). On the other hand, the effective surface area of the cathode did not change significantly (Figure S12)). Therefore, the hysteresis at the cathode can be explained by a structural change in the aluminium oxide layer as hydrolysis occurred at the cathode surface as the current density was changed, resulting in a lower overpotential necessary to drive the same current density.

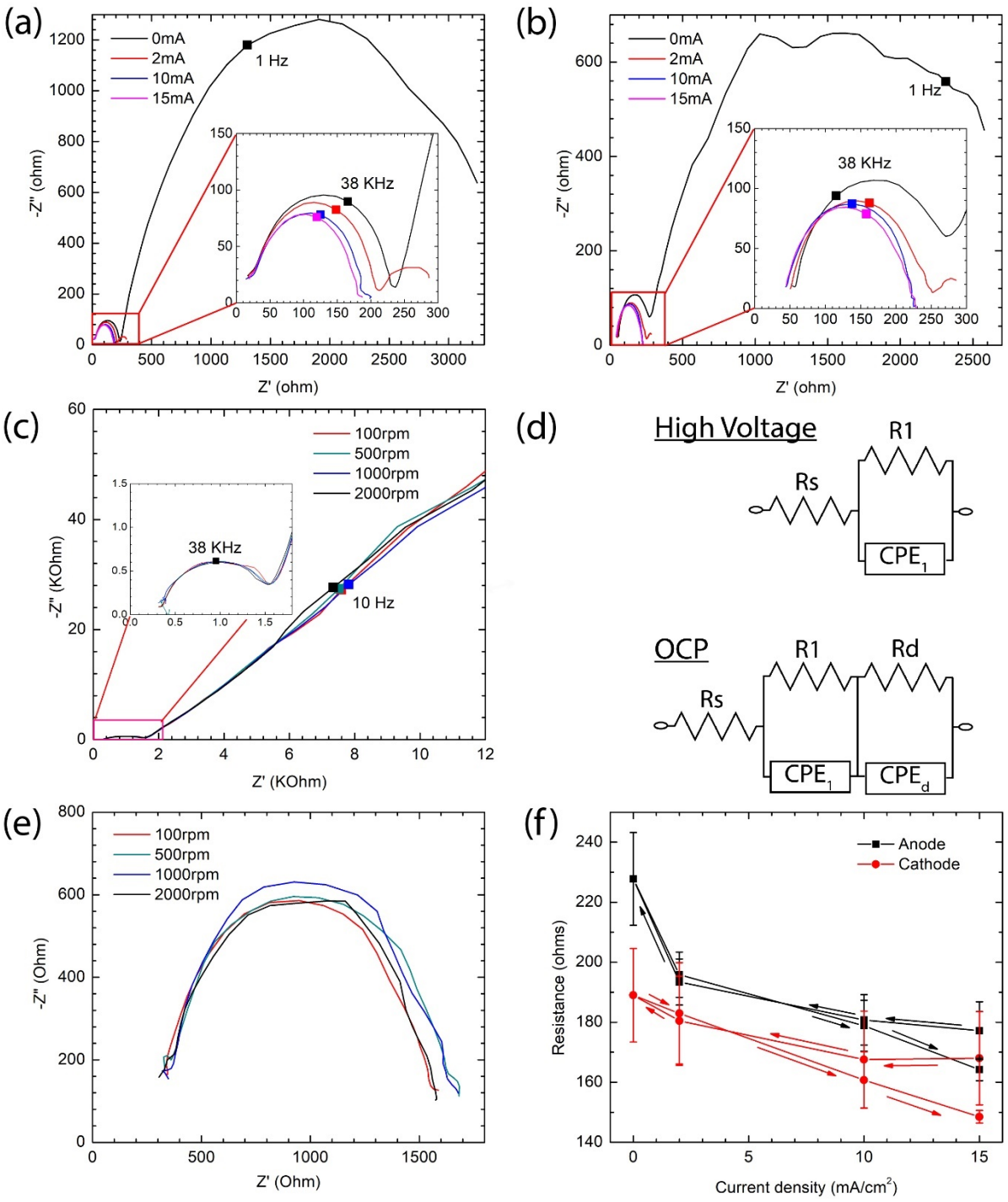

Figure 5: Nyquist plots of the Al (a) anode and (b) cathode at various current densities. (c) Nyquist plots of the Al anode at OCP using an RDE at different rotation speeds. (d) Equivalent circuit model used to fit the EIS experimental data at both high voltage and at OCP. (e) Nyquist plots of the Al anode at 15 mA/cm^2 using an RDE at different rotation speeds. (f) R1 values of the Al anode and cathode at various current densities.

Conclusion

An EC process in synthetic groundwater was explored using 5052 aluminium alloy electrodes in a flow-by cell with very short retention times (from 0.73 s up to 2.1 s) at current densities of 2, 10 and 25 mA/cm^2. Silica and hardness removal improved with increased current densities

and longer retention times owing to higher total aluminium concentration and floc formation. The removal of Si reached 50 ± 4%, and hardness removal reached 11 ± 1 % when EC was operated at 25 mA/cm^2 with a retention time of 2.1 s.

It was shown that in order to maintain a constant current density during EC of synthetic groundwater, more energy was required to be drawn by the anode rather than the cathode. Although there was scaling and bubble formation at the cathode, a layer of relatively more electrically conductive gibbsite formed on the cathode surface. The anode on the other hand had constant surface properties. After an initiation period where corrosion occurred (Figure S12), the anode's surface area stabilizes and remains constant. In addition to anodic corrosion, the dissolution of aluminium from the cathode (a result of high pH aluminium hydrolysis) contributes to dissolved aluminium concentrations in the reactor. The charge transfer resistances measured by EIS at the electrodes showed good correlation with changes in energy consumption of the two electrodes over time. The difference in the energy consumption trends of the two electrodes is attributed to a difference in aluminium dissolution mechanisms. While aluminium dissolution at the anode was electrochemical (i.e., controlled by anodic oxidation), dissolution of aluminium at the cathode was through hydrolysis that led to the formation of gibbsite that has been shown to be more electrically conducting than Al_2O_3. High mass transfer rates in the flow-by cell minimized the formation of thick amorphous $Al(OH)_3$ on the electrodes that could lead to higher energy consumption. As a result, an increase in the overpotential necessary to drive the required current density was minimized.

From EIS measurements at different current densities, it was shown that the resistance to charge transfer decreases with increased current densities. Resistance caused by the diffusion of aluminium ions or electrons through the aluminium oxide layer also disappears when the current density is raised above 2 mA/cm^2. The decrease in charge transfer resistance corresponds with the non-linear relationship between current and overpotential observed by Tafel.

Acknowledgement

Funding for this project was generously provided by the National Alliance for Water Innovation (award number 7550026).

Supporting Information

Supporting information, including detailed COMSOL simulation results, Siliaca and hardness removal data, and more electron microscopy images of the electrode surfaces are available. This material is available free of charge via the internet at http://pubs.acs.org.

Reference

1. Association, N.N.G.W. *Groundwater Use in the U.S.A.* 2020 13 January 2020; Available from: https://www.ngwa.org/docs/default-source/default-document-library/groundwater/usa-groundwater-use-fact-sheet.pdf?sfvrsn=5c7a0db8_4.
2. Afonso, M.D., J.O. Jaber, and M.S. Mohsen, *Brackish groundwater treatment by reverse osmosis in Jordan.* Desalination, 2004. **164**(2): p. 157-171.
3. Sang, Y., et al., *Heavy metal-contaminated groundwater treatment by a novel nanofiber membrane.* Desalination, 2008. **223**(1): p. 349-360.
4. Khor, C.M., et al., *Electrically Mediated Membrane Pore Gating via Grafted Polymer Brushes.* ACS Materials Letters, 2019. **1**(6): p. 647-654.
5. Belkacem, M., S. Bekhti, and K. Bensadok, *Groundwater treatment by reverse osmosis.* Desalination, 2007. **206**(1-3): p. 100-106.
6. Rao, U., et al., *Mineral scale prevention on electrically conducting membrane distillation membranes using induced electrophoretic mixing.* Environmental science & technology, 2020. **54**(6): p. 3678-3690.
7. Zhu, X., et al., *Field-induced redistribution of surfactants at the oil/water interface reduces membrane fouling on electrically conducting carbon nanotube UF membranes.* Environmental science & technology, 2018. **52**(20): p. 11591-11600.
8. Long, Y., et al., *Synergistic fouling behaviors and mechanisms of calcium ions and polyaluminum chloride associated with alginate solution in coagulation-ultrafiltration (UF) process.* Water Research, 2021. **189**: p. 116665.
9. Ohno, K., et al., *NF membrane fouling by aluminum and iron coagulant residuals after coagulation–MF pretreatment.* Desalination, 2010. **254**(1): p. 17-22.
10. Deka, B.J., et al., *Emerging investigator series: control of membrane fouling by dissolved algal organic matter using pre-oxidation with coagulation as seawater pretreatment.* Environmental Science: Water Research & Technology, 2020. **6**(4): p. 935-944.
11. Edzwald, J., *Coagulation in drinking water treatment: particles, organics and coagulants.* Water Science and Technology, 1993. **27**(11): p. 21-35.
12. Chen, S., T. Chang, and C. Lin, *Silica pretreatment for a RO brackish water source with high magnesium.* Water Science and Technology: Water Supply, 2006. **6**(4): p. 179-187.
13. Feng, L., et al., *Coagulation performance and membrane fouling of different aluminum species during coagulation/ultrafiltration combined process.* Chemical Engineering Journal, 2015. **262**: p. 1161-1167.
14. Tang, X., et al., *Chemical coagulation process for the removal of heavy metals from water: a review.* Desalination and Water Treatment, 2016. **57**(4): p. 1733-1748.
15. Amran, A.H., et al., *Effectiveness of natural coagulant in coagulation process: a review.* International Journal of Engineering & Technology, 2018. **7**(3.9): p. 34-37.
16. Song, Z., C.J. Williams, and R.G.J. Edyvean, *Treatment of tannery wastewater by chemical coagulation.* Desalination, 2004. **164**(3): p. 249-259.
17. Alexander, J.T., F.I. Hai, and T.M. Al-aboud, *Chemical coagulation-based processes for trace organic contaminant removal: Current state and future potential.* Journal of Environmental Management, 2012. **111**: p. 195-207.
18. Lacasa, E., et al., *Removal of nitrates from groundwater by electrocoagulation.* Chemical Engineering Journal, 2011. **171**(3): p. 1012-1017.
19. Gregor, J.E., C.J. Nokes, and E. Fenton, *Optimising natural organic matter removal from low turbidity waters by controlled pH adjustment of aluminium coagulation.* Water Research, 1997. **31**(12): p. 2949-2958.
20. Sher, F., A. Malik, and H. Liu, *Industrial polymer effluent treatment by chemical coagulation and flocculation.* Journal of Environmental Chemical Engineering, 2013. **1**(4): p. 684-689.

21. Mansouri, K., et al., *Anodic Dissolution of Pure Aluminum during Electrocoagulation Process: Influence of Supporting Electrolyte, Initial pH, and Current Density.* Industrial & Engineering Chemistry Research, 2011. **50**(23): p. 13362-13372.
22. Picard, T., et al., *Cathodic dissolution in the electrocoagulation process using aluminium electrodes.* Journal of Environmental Monitoring, 2000. **2**(1): p. 77-80.
23. Khan, S.U., M.S. Mahtab, and I.H. Farooqi, *Enhanced lead (II) removal with low energy consumption in an electrocoagulation column employing concentric electrodes: process optimisation by RSM using CCD.* International Journal of Environmental Analytical Chemistry, 2021: p. 1-18.
24. Malakootian, M. and N. Yousefi, *The efficiency of electrocoagulation process using aluminum electrodes in removal of hardness from water.* Journal of Environmental Health Science & Engineering, 2009. **6**(2): p. 131-136.
25. Ghosh, D., H. Solanki, and M.K. Purkait, *Removal of Fe(II) from tap water by electrocoagulation technique.* Journal of Hazardous Materials, 2008. **155**(1): p. 135-143.
26. Ali, I., T.A. Khan, and M. Asim, *Removal of arsenate from groundwater by electrocoagulation method.* Environmental Science and Pollution Research, 2012. **19**(5): p. 1668-1676.
27. Iddya, A., et al., *Efficient ammonia recovery from wastewater using electrically conducting gas stripping membranes.* Environmental Science: Nano, 2020. **7**(6): p. 1759-1771.
28. Hamdan, S.S. and M.H. El-Naas, *Characterization of the removal of Chromium (VI) from groundwater by electrocoagulation.* Journal of Industrial and Engineering Chemistry, 2014. **20**(5): p. 2775-2781.
29. Moussavi, G., R. Khosravi, and M. Farzadkia, *Removal of petroleum hydrocarbons from contaminated groundwater using an electrocoagulation process: Batch and continuous experiments.* Desalination, 2011. **278**(1): p. 288-294.
30. FENG, Q.-y., et al., *Removal of humic acid from groundwater by electrocoagulation.* Journal of China University of Mining and Technology, 2007. **17**(4): p. 513-520.
31. Bao, J., et al., *Removal of perfluoroalkanesulfonic acids (PFSAs) from synthetic and natural groundwater by electrocoagulation.* Chemosphere, 2020. **248**: p. 125951.
32. Mahmad, M.K.N., et al., *Electrocoagulation Process by Using Aluminium and Stainless Steel Electrodes to Treat Total Chromium, Colour and Turbidity.* Procedia Chemistry, 2016. **19**: p. 681-686.
33. Dubrawski, K.L., M. Fauvel, and M. Mohseni, *Metal type and natural organic matter source for direct filtration electrocoagulation of drinking water.* Journal of Hazardous Materials, 2013. **244-245**: p. 135-141.
34. KALIVEL, P., V. MOSES, and J. PALANICHAMY, *OPTIMIZATION OF COLOR REMOVAL OF BLUE SI DYE SOLUTION WITH Al-Al, Cu-Cu ELECTRODES IN ELECTROCOAGULATION PROCESS USING STATISTICAL MODELLING.*
35. Millar, G.J., et al., *Evaluation of electrocoagulation for the pre-treatment of coal seam water.* Journal of Water Process Engineering, 2014. **4**: p. 166-178.
36. Khor, C.M., et al., *Performance, Energy and Cost of Produced Water Treatment by Chemical and Electrochemical Coagulation.* Water, 2020. **12**(12): p. 3426.
37. Demirbas, E. and M. Kobya, *Operating cost and treatment of metalworking fluid wastewater by chemical coagulation and electrocoagulation processes.* Process Safety and Environmental Protection, 2017. **105**: p. 79-90.
38. Hashim, K.S., et al., *Iron removal, energy consumption and operating cost of electrocoagulation of drinking water using a new flow column reactor.* Journal of Environmental Management, 2017. **189**: p. 98-108.
39. Tahreen, A., M.S. Jami, and F. Ali, *Role of electrocoagulation in wastewater treatment: A developmental review.* Journal of Water Process Engineering, 2020. **37**: p. 101440.
40. Shahedi, A., et al., *A review on industrial wastewater treatment via electrocoagulation processes.* Current Opinion in Electrochemistry, 2020. **22**: p. 154-169.

41. El-Ashtoukhy, E.S.Z., et al., *Intensification of a new electrocoagulation system characterized by minimum energy consumption and maximum removal efficiency of heavy metals from simulated wastewater.* Chemical Engineering and Processing - Process Intensification, 2020. **154**: p. 108026.
42. Arambarri, J., B. Abbassi, and P. Zytner, *Enhanced removal of phosphorus from wastewater using sequential electrocoagulation and chemical coagulation.* Water, Air, & Soil Pollution, 2019. **230**(12): p. 1-9.
43. Mechelhoff, M., G.H. Kelsall, and N.J.D. Graham, *Electrochemical behaviour of aluminium in electrocoagulation processes.* Chemical Engineering Science, 2013. **95**: p. 301-312.
44. Harris, K.R. and L.A. Woolf, *Pressure and temperature dependence of the self diffusion coefficient of water and oxygen-18 water.* Journal of the Chemical Society, Faraday Transactions 1: Physical Chemistry in Condensed Phases, 1980. **76**: p. 377-385.
45. Ribeiro, A.C.F., et al., *Diffusion coefficients of aluminium chloride in aqueous solutions at 298.15, 303.15 and 315.15K.* Electrochimica Acta, 2007. **52**(23): p. 6450-6455.
46. Vik, E.A., et al., *Electrocoagulation of potable water.* Water Research, 1984. **18**(11): p. 1355-1360.
47. Pyun, S.-I. and S.-M. Moon, *Corrosion mechanism of pure aluminium in aqueous alkaline solution.* Journal of Solid State Electrochemistry, 2000. **4**(5): p. 267-272.
48. Venkatasubramanian, G., S. Mideen, and A.K. Jha, *Effect of pH on the corrosion behavior of aluminium alloy welded plate in chloride solutions.* Research Journal of Chemical Sciences _____ ISSN, 2013. **2231**: p. 606X.
49. Zhang, J., M. Klasky, and B.C. Letellier, *The aluminum chemistry and corrosion in alkaline solutions.* Journal of Nuclear Materials, 2009. **384**(2): p. 175-189.
50. Cañizares, P., et al., *Comparison of the aluminum speciation in chemical and electrochemical dosing processes.* Industrial & engineering chemistry research, 2006. **45**(26): p. 8749-8756.
51. Lekhlif, B., et al., *Study of the electrocoagulation of electroplating industry wastewaters charged by nickel (II) and chromium (VI).* J. Mater. Environ. Sci, 2014. **5**(1): p. 111-120.
52. Pitre, D., A. Boullemant, and C. Fortin, *Uptake and sorption of aluminium and fluoride by four green algal species.* Chemistry Central Journal, 2014. **8**(1): p. 1-7.
53. Perrault, G., *The role of hydrides in the equilibrium of aluminum in aqueous solutions.* Journal of the Electrochemical Society, 1979. **126**(2): p. 199.
54. Do, J.-S. and M.-L. Chen, *Decolourization of dye-containing solutions by electrocoagulation.* Journal of applied electrochemistry, 1994. **24**(8): p. 785-790.
55. McMaster-Carr. *Polished Easy-to-Weld 5052 Aluminum*. 2021 [cited 2021 7/19]; Available from: https://www.mcmaster.com/8199K106/.
56. Ingelsson, M., N. Yasri, and E.P. Roberts, *Electrode passivation, faradaic efficiency, and performance enhancement strategies in electrocoagulation—a review.* Water Research, 2020. **187**: p. 116433.
57. Donatus, U., et al., *Corrosion pathways in aluminium alloys.* Transactions of Nonferrous Metals Society of China, 2017. **27**(1): p. 55-62.
58. Tabrizi, M.R., et al., *The long-term corrosion of aluminium in alkaline media.* Corrosion Science, 1991. **32**(7): p. 733-742.
59. Armstrong, R. and V. Braham, *The mechanism of aluminium corrosion in alkaline solutions.* Corrosion Science, 1996. **38**(9): p. 1463-1471.
60. Parks, J.E., *Ohms Law III Resistors in Series and Parallel.* Department of Physics and Anatomy, University of Tennessee, 2007.
61. Brown, O.R. and J.S. Whitley, *Electrochemical behaviour of aluminium in aqueous caustic solutions.* Electrochimica Acta, 1987. **32**(4): p. 545-556.

62. Goswami, K.N. and A.K. Gupta, *A Study of Thermal Reactions of Gibbsite by Electrical Conductivity Measurements.* Transactions of the Indian Ceramic Society, 1977. **36**(2): p. 21-25.
63. Juyana, A.W. and M.N.B. Derman. *Characterization of porous anodic aluminium oxide film on aluminium templates formed in anodizing process*. in *Advanced Materials Research*. 2011. Trans Tech Publ.
64. Shon, H.K., et al., *Preparation of titanium oxide, iron oxide, and aluminium oxide from sludge generated from Ti-salt, Fe-salt and Al-salt flocculation of wastewater.* Journal of Industrial and Engineering Chemistry, 2009. **15**(5): p. 719-723.
65. Rashad, M., et al., *Effect of Graphene Nanoplatelets addition on mechanical properties of pure aluminum using a semi-powder method.* Progress in Natural Science: Materials International, 2014. **24**(2): p. 101-108.
66. Cesteros, Y., et al., *Several Factors Affecting Faster Rates of Gibbsite Formation.* Chemistry of Materials, 1999. **11**(1): p. 123-129.
67. Favaro, L., et al., *Experimental and ab initio infrared study of χ-, κ- and α-aluminas formed from gibbsite.* Journal of Solid State Chemistry, 2010. **183**(4): p. 901-908.
68. Runge, J.M., *Polarization: the key to anodic oxide formation.* Materials Today: Proceedings, 2019. **10**: p. 360-367.
69. Cimpoeşu, N., et al., *Electrochemical Characterization of a New Biodegradable FeMnSi Alloy Coated with Hydroxyapatite-Zirconia by PLD Technique.* Journal of Chemistry, 2016. **2016**: p. 9520972.
70. Deepa, P. and R. Padmalatha, *Corrosion behaviour of 6063 aluminium alloy in acidic and in alkaline media.* Arabian Journal of chemistry, 2017. **10**: p. S2234-S2244.
71. Branzoi, V., F. Golgovici, and F. Branzoi, *Aluminium corrosion in hydrochloric acid solutions and the effect of some organic inhibitors.* Materials Chemistry and Physics, 2003. **78**(1): p. 122-131.
72. Wardan, R., et al. *Effects of different pH of 3.5% NaCl solution on steel under zero charge corrosion protection technique*. in *Journal of Physics: Conference Series*. 2021. IOP Publishing.
73. Zelinsky, A. and B.Y. Pirogov, *Effective thickness of the diffusion layer during hydrogen ion reduction in aqueous hydrochloric acid solutions.* Russian Journal of Electrochemistry, 2008. **44**(5): p. 585-593.
74. Allen, J.B. and R.F. Larry, *Electrochemical methods fundamentals and applications*. 2001: John Wiley & Sons.
75. Yuan, X.-Z., et al., *EIS equivalent circuits.* Electrochemical Impedance Spectroscopy in PEM Fuel Cells: Fundamentals and Applications, 2010: p. 139-192.
76. Mibus, M., et al., *Dielectric breakdown and failure of anodic aluminum oxide films for electrowetting systems.* Journal of Applied Physics, 2013. **114**(1): p. 014901.
77. Gileadi, E. and E. Kirowa-Eisner, *Some observations concerning the Tafel equation and its relevance to charge transfer in corrosion.* Corrosion Science, 2005. **47**(12): p. 3068-3085.
78. Scott, K., *Electrochemical principles and characterization of bioelectrochemical systems*, in *Microbial Electrochemical and Fuel Cells*. 2016, Elsevier. p. 29-66.
79. Khan, S.U.M., R.C. Kainthla, and J.O.M. Bockris, *The redox potential and the Fermi level in solution.* The Journal of Physical Chemistry, 1987. **91**(23): p. 5974-5977.